Noname manuscript No.
(will be inserted by the editor)

Large-Eddy-Simulation Study on the Effects of Building-Height Variability on Turbulent Flows over an Actual Urban Area

Toshiya Yoshida · Tetsuya Takemi · Mitsuaki Horiguchi

Received: DD Month YEAR / Accepted: DD Month YEAR

Abstract A large-eddy simulation (LES) was conducted to investigate the effects of building-height variability on turbulent flows over an actual urban area, the city of Kyoto, which was reproduced using a 2-m resolution digital surface dataset. Comparison of the morphological characteristics of Kyoto with those of European, North American, and other Japanese cities indicates a similarity to European cities but with more variable building heights. The performance of the LES model is validated and found to be consistent with turbulence observations obtained from a meteorological tower and Doppler lidar. We conducted the following two numerical experiments: a control experiment using Kyoto buildings, and a sensitivity experiment in which all the building heights are set to the average height over the computational region h_{all}. The difference of Reynolds stress at

Toshiya yoshida · Tetsuya Takemi · Mitsuaki Horiguchi

Disaster Prevention Research Institute, Kyoto University, Kyoto, Japan

E-mail: yoshida_t@storm.dpri.kyoto-u.ac.jp

height $z = 2.5h_{all}$ between the control and sensitivity experiments is found to increase with the increase in the plan-area index (λ_p) for $\lambda_p > 0.32$. Thus, values of λ_p of around 0.3 can be regarded as a threshold for distinguishing the effects of building-height variability. The quadrant analysis reveals that sweeps contribute to the increase in the Reynolds stress in the control experiment at height $z = 2.5h_{all}$. The exuberance in the control experiment at height $z = 0.5h_{all}$ is found to decrease with an increase in the building-height variability. Although the extreme momentum flux at height $z = 2.5h_{all}$ in the control experiment appears around buildings, it contributes little to the total Reynolds stress and is not associated with coherent motion.

Keywords Actual urban building · Large-eddy simulation · Atmospheric turbulence · Roughness parameter · Reynolds stress · Quadrant analysis

1 Introduction

Atmospheric processes over urban areas are affected not only by meteorological disturbances, such as thunderstorms, fronts, and cyclones, but also by the roughness and thermal effects of buildings and man-made structures. The geometrical features of buildings and structures determine the roughness effects of an urban area, while human activities and the material characteristics of buildings play a role in defining the thermal effects of such areas. The complex geometrical nature of urban surfaces results in highly complex turbulent flows. To properly understand the physical processes of momentum and heat transfer in urban areas and develop parametrizations for urban environments in numerical weather prediction models, it is important to reveal relationships between the effects of actual urban buildings and turbulent flows.

The characteristics of turbulent flows over urban surfaces have been examined in numerous previous studies. Oke (1988) categorized the airflow over roughness obstacles as a function of obstacle density as isolated flows, wake-interference flows, and skimming flows. Macdonald et al. (1998) derived a theoretical relation for the aerodynamic roughness length z_0 and displacement height d for flows over roughness blocks. While these studies examined turbulent flows over roughness blocks with constant height and regular distribution, the recent focus has shifted to the effects on turbulent flows of roughness blocks with variable height and inhomogeneous arrangement. Wind-tunnel experiments conducted by Cheng and Castro (2002) demonstrated that the roughness sublayers over block arrays with random height are thicker than those over uniform-height arrays. Xie et al. (2008) conducted a large-eddy simulation (LES) of turbulent flows over block arrays with random height, and found that the tall blocks significantly contribute to the total drag of such arrays. Nakayama et al. (2011) performed LES investigations over building arrays with different height variability and found that the vertical profiles of the mean velocity and Reynolds stress depend significantly on the building-height variability. Zaki et al. (2011) performed wind-tunnel experiments with block arrays of buildings with variable height distributed randomly, and showed that the drag coefficient C_d increases with the building density and the standard deviation of the building height for high building densities. Numerical simulations of plume dispersion over urban surfaces have revealed that the turbulence is significantly affected by the source location and wind direction because of the strong dependence on the building height and distribution. (Xie and Castro 2009; Xie 2011;

Nakayama et al. 2016). The parametrizations of z_0 and d have been improved by taking into account roughness parameters associated with actual urban buildings, such as the maximum, standard deviation, and skewness of the building height (Nakayama et al. 2011; Kanda et al. 2013; Zhu et al. 2017). Giometto et al. (2016) suggested that the dispersive flux derived from spatial variations of temporal mean flows around buildings should be considered to improve conventional urban-canopy parametrizations.

To fully understand the effects of roughness obstacles on turbulent flows, it is helpful to investigate the relationships between turbulent organized structures and obstacles, because organized structures are associated with downwards momentum transfer in the form of ejection and sweep events based on a quadrant analysis for the turbulent momentum flux. The results of wind-tunnel experiments on flows over rough surfaces conducted by Raupach (1981) indicate that sweeps are dominant for the total momentum flux near surfaces, and that the contribution of ejection to the momentum flux increases with height. Studies in which turbulence was observed over actual urban areas have revealed the characteristics of momentum transfer and coherent motion. Oikawa and Meng (1995) observed turbulent structures associated with ejections and sweeps over an urban area, and found that turbulent structures correlate with heat transfer within and above the urban canopy. Christen et al. (2007) analyzed field experimental data obtained from sonic-anemometer measurements within and above a street canyon in Basel, Switzerland, and found that sweeps are mostly dominant up to a height of approximately twice the average building height in a street canyon. Numerical simulations of flows over building arrays have revealed the spatial characteristics of turbulent organized structures. Kanda et al. (2004) carried out LES investigations of turbulent flows over uniform-height block arrays to investigate turbulent organized structures over such arrays. They found low-speed streaks and streamwise vortices similar to those in flows over flat-wall boundary layers. Kanda (2006) indicated that streak structures are a common feature over various types of block arrays. Using direct numerical simulations, Coceal et al. (2007a,b) revealed that hairpin vortices associated with ejections and sweeps are generated over uniform block arrays, and that the low-speed streaks identified above such arrays are composed of large numbers of hairpin vortices aligned in the streamwise direction. Park et al. (2015) used LES results to analyze turbulent-flow structures over an actual urban area in Seoul, Korea, and showed that turbulent structures behind high-rise buildings are characterized by streamwise vortices with strong ejections. They focused on small regions containing high-rise buildings, and demonstrated the significant influence of high-rise buildings on wake flows. The majority of studies presented thus far have focused on the characteristics of turbulent flows over idealized or specific buildings, while only a few have examined the urban-scale effects on the characteristics of turbulent momentum transfer produced by the complex geometrical features of actual urban surfaces.

The geometrical characteristics of actual urban surfaces can be reproduced from digital surface datasets. Ratti et al. (2002) calculated the roughness parameters of North American and European cities, and found that parameters differ significantly by city. Bou-Zeid et al. (2009) indicated that turbulent flows are dependent on the building representation over the actual urban surface. To understand the characteristics of turbulent flows over urban areas, it is therefore important to use the geometry of actual buildings in simulations and experiments.

We investigate here the effects of building-height variability in an actual urban area on turbulent flows at an urban scale, focusing on the airflow within and above an urban-canopy layer, where turbulent flows are strongly influenced by individual buildings.

We simulate the turbulent flow over the urban area of Kyoto, which is characterized by the presence of both business districts with high buildings and densely built residential districts. Furthermore, a meteorological observation tower owned by Kyoto University and located in the southern part of the city can be used for the validation of simulations. In Sect. 2, the building morphological characteristics of Kyoto are evaluated using roughness parameters. The details of our LES model are described in Sect. 3. The study area of the LES investigation is defined to include the meteorological tower site at which turbulence was measured by a sonic anemometer and Doppler lidar, so that LES results may be compared with the observations (see Sect. 4). Along with a control simulation, we conduct a sensitivity test assuming a constant building height to reveal the effects of building height–height variability, with the differences between the control and sensitivity experiments examined in Sect. 5. Finally, Sect. 6 concludes the paper.

2 Building Morphological Characteristics of Kyoto

Our study area covered both business districts and suburban areas in Kyoto. Figure 1 shows the area of interest in Kyoto, which extends 11 km in a north–south direction and by 2 km in an east–west direction. A digital surface model (Kokusai Kogyo Co., Ltd.) was used to reproduce the actual urban buildings within a numerical model. The original 2-m-resolution data are smoothed and converted to a 4-m resolution, which is used as the horizontal grid spacing of the numerical experiments as described in Sect. 3.2.

Figure 2a shows the height of the actual buildings in the analysis area. The north–south and west–east directions are referred to as the x and y directions, respectively. The region with $x = 0 - 4$ km corresponds to the city centre of Kyoto. The heights of almost all buildings in the region are up to 50 m, and there are no high-rise building clusters of the type seen in the centre of Tokyo. The region for $x = 7 - 11$ km is primarily occupied by suburban areas and rivers.

The difference between the building heights over these two regions is clearly indicated in Fig. 2b, which shows the frequency distributions of building heights over the entire analysis area and in the $x = 0 - 4$ km and $x = 7 - 11$ km regions. In calculating the frequency distributions, all buildings are defined as having heights of at least 1 m to distinguish between the buildings and the ground. It is seen that most of the buildings taller than 25 m are located in the former region.

To quantitatively indicate the morphological characteristics of buildings in Kyoto, we use roughness parameters such as the average building height H_{ave}, the standard deviation of the building height σ_H, the plan-area index λ_p (the ratio of the plan area occupied by buildings to the total surface area), and the frontal-area index λ_f (the ratio of the frontal area of buildings to the total surface area). These parameters are calculated for each 1 km by 1 km area following the analysis of Kanda et al. (2013). Figure 3a shows λ_p calculated in the areas of 1 km by 1 km for the buildings shown in Fig. 2a, with the values of the roughness parameters in the 1 km by 1 km areas summarized in Fig. 3b. The average values of H_{ave}, σ_H, λ_p, and λ_f over the $x = 0 - 4$ km region are 10.8, 7, 0.41, and 0.25, respectively, while the corresponding averages over $x = 7 - 11$ km are 9.8, 5.3, 0.2, and 0.16, respectively. Thus, the $x = 0 - 4$ km region is more densely built than the $x = 7 - 11$ km. Using building data from Tokyo and Nagoya, Japan, Kanda et al. (2013) derived the following empirical relationships between λ_p and λ_f, and between H_{ave} and σ_H,

$$\lambda_f = 1.42\lambda_p^2 + 0.4\lambda_p, \tag{1}$$

$$\sigma_H = 1.05H_{ave} - 3.7. \tag{2}$$

Figure 3c and d indicates the respective relationships between λ_p and λ_f, and between H_{ave} and σ_H, based on the data given in Fig. 3b. Also shown in the panels are the empirical relationships of Kanda et al. (2013) and the data for North American and European cities found in Ratti et al. (2002). For $\lambda_p > 0.3$, the λ_f values for Kyoto tend to be smaller than in the empirical profile. This feature of Kyoto appears to be similar to those seen in European cities, and indicates that the fraction of high buildings in Kyoto is limited relative to those in major metropolitan cities in Japan and North America. The relationship between H_{ave} and σ_H for Kyoto is in good agreement with those of Tokyo and Nagoya, but differs from those of European cities. Finally, the magnitudes of H_{ave} and σ_H in Kyoto are smaller than those of Los Angeles by a factor of $5 - 10$.

According to these results, Kyoto can be morphologically characterized as having densely distributed buildings with widely varying heights. The Kyoto dataset was used for the numerical simulations described in the next section.

3 Numerical Model and Experimental Design

3.1 Numerical Model

Our LES model is effectively the same as the one used in Nakayama et al. (2011), except that it neglects the molecular viscosity term, and employs a bottom boundary condition based on Monin–Obukhov similarity theory, as described later. In Nakayama et al. (2011), the performance of the LES model reproducing turbulent statistics was validated using data obtained from wind-tunnel experiments; as a close agreement was found, the model developed by Nakayama et al. (2011) has subsequently been applied to simulate turbulent flows over actual urban cities. Nakayama et al. (2012) conducted LES investigations of turbulent flows over Tokyo by coupling their model with a mesoscale meteorological model, and found that observed gust factors are accurately reproduced by the model. The model was also used to successfully reproduce the wind speeds and directions at the ground level in the Fukushima Daiichi Nuclear Power Plant during the Great East Japan Earthquake and its aftermath in March 2011 (Nakayama et al., 2015). Nakayama et al. (2016) further applied their LES model for the simulation of turbulent flows and plume dispersion over Oklahoma City, and showed that the observed characteristics of turbulence and dispersion are reproduced despite the fact that small differences in wind direction caused by the building distribution significantly influenced the plume dispersion. Thus, our LES model has been widely tested and is applicable for the analysis of the turbulent flow over Kyoto.

The LES model solves the filtered continuity and Navier–Stokes equations in Cartesian coordinates with the subgrid-scale stress parametrized by the standard Smagorinsky model (Smagorinsky, 1963). The governing equations are

$$\frac{\partial \tilde{u}_i}{\partial x_i} = 0, \tag{3}$$

$$\frac{\partial \tilde{u}_i}{\partial t} + \tilde{u}_j \frac{\partial \tilde{u}_i}{\partial x_j} = -\frac{1}{\rho}\frac{\partial \tilde{p}^*}{\partial x_i} - \frac{\partial \tau_{ij}}{\partial x_j} + f_i, \tag{4}$$

$$\tau_{ij} - \frac{1}{3}\delta_{ij}\tau_{kk} = -2(C_s \Delta)^2 (2\tilde{S}_{ij}\tilde{S}_{ij})^{1/2}\tilde{S}_{ij}, \tag{5}$$

$$\tilde{S}_{ij} = \frac{1}{2}\left(\frac{\partial \tilde{u}_i}{\partial x_j} + \frac{\partial \tilde{u}_j}{\partial x_i}\right), \tag{6}$$

where t denotes time, $\tilde{u}_i$ is the filtered air velocity in the direction i, $\tilde{p}^* = \tilde{p} + \frac{1}{3}\rho\tau_{kk}$ is the modified pressure, $\tilde{p}$ is the filtered pressure, ρ is the density of air, τ_{ij} is the subgrid-scale stress, δ_{ij} is the Kronecker delta, $\tilde{S}_{ij}$ is the filtered stress tensor, and f_i is the external force exerted by roughness obstacles. The parameter x_i represents the coordinate system, with components $i = 1,\ 2$, and 3 referring to the streamwise (x), spanwise (y) and vertical (z) directions, respectively. In addition, $\Delta = (\Delta_x \Delta_y \Delta_z)^{1/3}$ is the filter width, where Δ_x, Δ_y, and Δ_z are the streamwise, spanwise, and vertical grid spacings, respectively. The Smagorinsky coefficient C_s is set to 0.14. Note that the viscous term is neglected because our target is the simulation of turbulent flow with a high Reynolds number.

The external force f_i is used to simulate the effects of buildings on the flow, for which we employ the feedback forcing by Goldstein et al. (1993) who give

$$f_i = \alpha \int_0^t u_i(t')dt' + \beta u_i(t), \quad \alpha < 0,\ \beta < 0, \tag{7}$$

where α and β are negative constants. The stability limit is given by $\Delta t < \frac{-\beta - \sqrt{(\beta^2 - 2\alpha k)}}{\alpha}$, where k is a constant of order one. Following Nakayama et al. (2011), these constants are set as $\alpha = -10$, $\beta = -1$, and $k = 1$.

The governing equations are discretized on a staggered-grid system. The velocity and pressure fields are solved using a coupling method based on the marker-and-cell method (Chorin, 1967). The successive over-relaxation method is used to solve the Poisson equation for pressure, and the Adams–Bashforth scheme is adopted for the time integration. A second-order accurate, central-differencing scheme is employed for spatial discretization. The code is parallelized using a Message Passing Interface library to reduce the computational time.

3.2 Experimental Design

The governing equations are numerically solved in two computational domains: the driver region, which features regularly arrayed obstacles, and the main region, which contains the actual buildings of Kyoto. To ensure the flow field of the LES is turbulent, a turbulent flow is generated in the driver region and imposed as the inflow at the boundary of the main region. The concept involved in setting the driver and the main regions is demonstrated in Fig. 4. The size of the driver region is 6 km (streamwise) $\times$ 2.4 km (spanwise) $\times$ 1.015 km (vertical), with a grid spacing of 4 m in the horizontal directions, and a grid spacing stretched with increasing altitude from 1 m to 16 m in the vertical direction. The total number of grid points is 1500 $\times$ 600 $\times$ 105. In the driver region, there is one rectangular block aligned in the spanwise direction, and an array of roughness blocks staggered with $\lambda_p = 0.04$. The individual rectangular and roughness block sizes are 50 m $\times$ 2400 m $\times$ 50 m and 16 m $\times$ 16 m $\times$ 10 m, respectively. The purpose of setting the size of the rectangular block is to enhance perturbations near the inlet of the driver region. The λ_p value chosen for the block array is set to be a little larger than that in Nakayama et al. (2014) to reduce the generation of turbulence. The height of the blocks is chosen according to the mean building height in the main region.

A uniform flow with a velocity magnitude of 5 m s^{-1} is imposed at the inflow boundary of the driver region. The Sommerfeld radiation condition is imposed at the outflow boundary, while a periodic condition is set at the lateral boundaries. At the top boundary, free-slip and zero-speed conditions are imposed for the horizontal and vertical velocity components, respectively. At the ground, a boundary condition based on Monin–Obukhov similarity theory is employed. The stress at the first vertical grid $\tau_{i3}(x, y, t)$ is calculated as (Stoll and Porté-Agel, 2006)

$$\tau_{i3}(x, y, t) = -\left[\frac{\tilde{u}_r(x, y, z_s, t)\kappa}{\ln(z_s/z_0)}\right]^2 \frac{\tilde{u}_i(x, y, z_s, t)}{\tilde{u}_r(x, y, z_s, t)}, \tag{8}$$

where $\tilde{u}_r(x, y, z_s, t) = [\tilde{u}_1(x, y, z_s, t)^2 + \tilde{u}_2(x, y, z_s, t)^2]^{1/2}$ is the instantaneous resolved velocity magnitude, z_s is the altitude at the first vertical grid, z_0 is the roughness length, and κ is the von Kármán constant. Here, $z_0 = 0.1$ m (Bou-Zeid et al., 2009) and $\kappa = 0.4$.

The ratio of the boundary-layer height δ of the generated outflow to the roughness block height in the driver region is 27.9. Note that, here, δ is defined as the height at which the mean streamwise velocity component at the outflow indicates a peak value. In Nakayama et al. (2011), the ratio of δ to the roughness block height in the driver region is 13. In addition, we confirmed that the vertical profiles of the standard deviation of each velocity component and Reynolds stress are in reasonable agreement with those obtained from wind-tunnel experiments, although the LES results underestimate the spanwise and vertical components and Reynolds-stress values relative to the wind-tunnel results (see Online Resource 1, Figure 1).

These results suggest that well-developed, deep turbulent flows are generated in the driver region.

In the main region, the domain size and the total number of grid points are 12 km $\times$ 2.4 km $\times$ 1.015 km and 3000 $\times$ 600 $\times$ 105, respectively. The main region includes the actual buildings and structures in Kyoto, as shown in Fig. 2a. For computational purposes, we set a buffer area spanning 500 m and 200 m in the streamwise and spanwise directions, respectively, surrounding the actual building area in the main region (not shown in Fig. 2a). The streamwise width of the area was determined based on Nakayama et al. (2012), who carried out an LES investigation of the airflow over Tokyo. Whereas Nakayama et al. (2012) did not set a buffer area in the spanwise direction, we decided that a spanwise buffer is necessary to avoid building discontinuities arising from the periodic boundary conditions. In this buffer area, the same roughness blocks used in the driver region are applied to maintain a turbulent flow over roughness surfaces. Note that the coordinates $x = 0$ km and $y = 0$ km are set to the northern and western boundaries, respectively, of the actual building area in the main region. Correspondingly, the inflow boundary condition provided by the driver region is set at $x = -500$ m in the main region. Outside of the inflow boundary, the boundary conditions of the main region are the same as those in the driver region, and all grid spacings are identical to those in the driver region.

Hereafter, the simulation using the actual buildings in Kyoto is referred to as the control experiment (CTL). To reveal the effects of building-height variability, we conducted an additional experiment referred to as the uniform experiment (UNI) in which all building heights are set to the average of the actual building heights in the main region (h_{all} =10.3 m). The integration time for each of the two experiments is 7,200 s, with the results obtained from the last 1,800 s used for the analysis of turbulent statistics. In Sect. 4.3, we confirm that the flows were in equilibrium states during this analysis period, as shown Fig. 5. In addition, as seen in Fig. 1 of Online Resource 1, the second-order moments of the inflow profiles are relatively small compared with those of the wind-tunnel experiments, which possibly influences the results presented here. However, as the same inflow condition was applied in both the CTL and UNI experiments, we can assume that any differences in the respective experimental results are unaffected by this issue.

4 Comparison with Observations

4.1 Observational Setting

The observations were performed at the Ujigawa Open Laboratory of the Disaster Prevention Research Institute, Kyoto University, during the period from 12 January to 12 February 2016. The laboratory is located in the southern part of Kyoto, and is surrounded by low-rise buildings and structures. The location of the observation site is shown in Fig. 1, which includes a meteorological observation tower of height 55 m. This tower is a unique facility first deployed in 1978 (Nakajima et al., 1979), and is currently one of the few meteorological towers operating in Japan.

A sonic anemometer (DA-600, Kaijo Co.) installed on the tower at a 25-m height measures the three velocity components as well as the air temperature at a 10-Hz sampling rate. The surrounding area up to 500 m north of the tower has only low building heights (< 25 m), enabling the assumption that observations taken by the sonic anemometer are not influenced by the strong wakes of tall buildings.

We also installed a Doppler lidar (WINDCUBE WLS-7, Leosphere) at the ground near the tower, from which we obtained three-component velocity measurements at heights ranging from 40 m to 200 m with a 20-m interval at a sampling rate of 1 Hz.

4.2 Data Selection

The observation site was included in the main region assessed in the numerical experiment for the purpose of directly comparing the LES results in the CTL experiment with the observations. As the sonic anemometer installed on the tower faces northwards, we analyzed data for dominant northerly wind directions to minimize the interference from the tower. To extract suitable periods from the observational data, we imposed two criteria for sorting values obtained from the sonic anemometer. First, a northerly flow condition was adopted by classifying 10-min averaged wind directions into 16 classes and extracting periods when northerly wind directions $(348.25^\circ - 360^\circ, 0^\circ - 11.25^\circ)$ were sustained for at least 30 min. Note that the time period for the analysis of the LES data was also 30 min. Second, a neutrally stratified condition was chosen based on the Monin–Obukhov stability parameter

$$\frac{z}{L} = -\frac{(g/\overline{T})\overline{w'T'}}{u_*^3/\kappa z}, \tag{9}$$

so that the assumption of turbulent flows under a neutrally stratified condition in the LES model is valid. Here, L is the Obukhov length (m), g is the acceleration due to gravity (m s^{-2}), T is the air temperature (K), $\overline{w'T'}$ is the sensible heat flux (K m s^{-1}), and u_* is the friction velocity (m s^{-1}). An overbar and prime denote a temporal average and fluctuation, respectively. A period for $|z/L| \leq 0.05$ (Roth, 2000) is regarded as fulfilling the neutrally stratified condition.

By imposing the above conditions on the observational data, we obtained the following four 30-min periods: 0720 – 0750 LT (local time = UTC + 9 h) 22 January; 1650 – 1720 LT 30 January; 0740 – 0810 LT 2 February; and 1830 – 1900 LT 10 February, which are referred to as the D1, D2, D3, and D4 periods, respectively. The wind directions for each period calculated from the averaged horizontal velocity components are 4.9°, 358.8°, 353.8°, and 351.5° for the D1 to D4 periods, respectively.

To compare the LES results with the observations, it is necessary to use airflows observed at the Ujigawa Open Laboratory coming from the northern boundary of the analysis region of Kyoto passing through the analysis region, and not from the western or eastern boundaries. Because of the periodic conditions at the western and eastern boundaries, the flow through these lateral boundaries is unlikely to be accurately simulated by the LES model. This condition requires that wind directions be within a range of between approximately 355° and 5° based on the streamwise length and half the spanwise length of the analysis region (i.e., arctan(1 km/11 km)). Overall, the wind directions in the periods D1 – D4 are almost within the range of this condition, although those in the periods D3 and D4 are slightly shifted westwards from the condition. We confirmed that the area within at least 1 km westwards from the analysis region is dominated by land-use and building types similar to those in the analysis region. Thus, we concluded that the anemometer data taken during the four periods described above are appropriate for comparison with the LES results. However, the wind directions measure by the Doppler lidar deviate from those recorded by the sonic anemometer. The directions of the Doppler lidar in the D1 and D3 periods become more westerly with height, reaching 330° at a height of 200 m, while those in the D2 and D4 periods are relatively constant with altitude and within a range between approximately 350° and 0°. We discuss the possible influences of the variation of wind direction in Sect. 4.3. As explained above, none of the observed wind directions were oriented in a truly northerly fashion. Correspondingly, we rotated the streamwise directions to the mean of the wind directions measured by the sonic anemometer and the Doppler lidar.

4.3 Results

Figure 5a and b shows the time series of streamwise and spanwise velocity components produced by the LES model and measured by the sonic anemometer at a 25-m height, respectively. To avoid interference from the tower on the wind-speed profiles, the LES results are shown for a grid point 16 m north of the tower. It is seen that the LES turbulent fluctuations in both the streamwise and spanwise directions are quite comparable to those from the anemometer. Note that average spanwise velocity components are nearly zero, as indicated in Fig. 5b. The streamwise velocity component is stronger in the D2 period than in the other periods. Comparison of the respective weather charts for the four time periods reveals the stronger wind speeds in the D2 period to be caused by a large low-pressure system passing through the northwest Pacific Ocean off the coast of the Japanese Islands.

Figure 5c shows a comparison of the LES and observed vertical profiles of the mean streamwise velocity component. Both datasets are averaged over time, and the time-averaged LES data are averaged horizontally over a 16 m by 16 m area to the north of the tower to increase the representativeness of the simulated flows for the observation site. Note that, given the logarithmic scales used on both axes, the slopes of the mean streamwise velocity component in Fig. 5c suggest a power-law profile. According to Counihan (1975), the slopes of suburban and urban areas range between 0.21 and 0.28, making a power-law exponent of 1/4 suitable for reference, where it is seen that the slopes of the observations and the LES results are very similar to this value. We also examined the respective vertical profiles of the mean streamwise velocity component normalized by the mean streamwise velocity component at the 25-m height (see Online Resource 1, Figure 2) and found that the LES and observed mean streamwise velocity components are quantitatively consistent. We conclude that this result is also good evidence for the reasonable performance of our LES model. In contrast, the slopes above approximately the 150-m height in the D1, D2, and D3 periods appear to deviate from the reference slope. In the case of the D1 and D3 periods, we assume this occurs because of the change in wind direction from northerly to westerly, as described in the previous subsection. Another possible explanation for the deviation at the higher levels is that the stability conditions may not have been neutral at these heights during the observed periods. Because there were no observational data available to classify the stability condition above height of the sonic anemometer at 25 m, it is impossible to quantitatively reveal the stability above that height.

The vertical profiles of Reynolds stress in both the observations and the LES results are shown in Fig. 5d. Note that the Reynolds stress is normalized by the mean streamwise velocity components at each height. The Reynolds stress of the LES data is averaged horizontally over the same 16 m by 16 m area used for the mean streamwise velocity component. It is seen that the vertical profile of the LES data is within the range of differences found in the observation periods, which is a feature similar to that of the profiles normalized by the mean streamwise velocity component at the 25-m height (see Online Resource 1, Figure 2). However, it is necessary to be careful in comparing the LES results with the Doppler lidar data because the latter might include some errors in representing perturbations of the wind speed as discussed below.

We now compare the results for the turbulence intensity, which is the ratio of the standard deviation of each velocity component σ_i to the mean streamwise velocity component. As previously mentioned, the turbulence intensity was also averaged horizontally in the 16 m by 16 m area. Figure 6 compares the vertical profiles of turbulence intensity in the LES results and observations with the empirical form of the ESDU (1985), which is a database providing the turbulence characteristics of a neutrally stratified atmospheric boundary layer based on various field measurements from around the world. In Fig. 6, all sonic-anemometer components fall within the rough-surface category given by the ESDU, which indicates suburban areas with z_0 between 0.1 and 0.5. Each component simulated by the LES model appears to capture the vertical distribution of that obtained by the ESDU within or around its upper and lower limits, at least below about the height of 150 m, while being slightly smaller than those of the sonic-anemometer observations. In fact, the values obtained from the sonic anemometer lie near the upper limit of the ESDU profile, suggesting that the LES results within the ESDU range are generally more favourable.

In contrast, there appears to be large discrepancies between the Doppler lidar observations and the LES results in terms of the u and v velocity components. The turbulence intensities for these components measured by the Doppler lidar are even larger than the upper limits of the ESDU, suggesting that the measurements may include an overestimating bias for the turbulence intensities. It is in fact commonly understood that the Doppler lidar measurements overestimate the turbulence intensities for the streamwise component. This characteristic was noted in Cañadillas et al. (2011), who showed that the results produced by the Doppler lidar observations are larger than those of sonic anemometers at various wind speeds and altitudes, and the deviations become larger with the decrease in wind speed. A close look at Figs. 5c and Fig. 6a indicates that the difference between Doppler lidar and the ESDU in terms of the streamwise turbulence intensity below 100 m decreases as the streamwise velocity conponent increases, in apparent confirmation of the finding of Cañadillas et al. (2011). For the Doppler lidar data above 100 m, changes in the wind direction and uncertainty in the stability, as revealed in the mean streamwise velocity component, may contribute to this overestimation. An overestimating tendency in the lidar data can also be found for the spanwise component, which has a mean value of nearly zero.

The vertical component produced by the LES results appears to be consistent with both the lidar data and the ESDU profile, but the lidar tends to underestimate the vertical turbulence intensity, particularly in weaker wind-speed conditions.

Figure 7 shows the power spectra of the time series of each velocity component obtained from the LES results and the sonic anemometer at a height of 25 m. The spectra were calculated from the time series shown in Fig. 5, and the frequency f and velocity spectra $E(f)$ are normalized in dimensionless form. The figure includes the empirical reference from Kaimal et al. (1972) derived from observations over a rural region. A close agreement is seen between the sonic anemometer and the reference results for all three components. The spectra from the sonic anemometer clearly represent an inertial subrange with a ?2/3 slope. Comparison of the LES spectra with the observations and empirical reference reveals that the spectra of the u and v components of the LES data are similar to those of the sonic anemometer data except in the highest frequency range. The lower frequency portion of the inertial subrange appears to be well reproduced for these components in the LES results.

However, the LES model is able to reproduce the vertical velocity components in only the lowest frequency portion of the inertial subrange. It is possible that the grid spacing used in our modelling is insufficient for resolving the smallest eddies and their corresponding vertical motion. Further increases in the vertical resolution may be required to represent the small-scale vertical motion likely to be induced at the edges of buildings. However, we note that the spectral peak of the w component in the LES results agrees well with that of the sonic anemometer.

From the above comparisons, we conclude that the use of our LES model leads to a reasonable reproduction of the turbulent boundary-layer flow over actual buildings under a neutral stability condition, at least up to a height of about 150 m. We emphasize that, in general, the results produced by our LES model agree favourably with the observations within the range of differences among the chosen periods (D1 – D4), even though our inflow condition employed an idealized turbulent flow generated in the driver region without realistic meteorological conditions. These results are sufficient here because our analysis of building-height variability focuses on altitudes below approximately 25 m (i.e., at height $z = 2.5h_{all}$), where the LES results show an especially close agreement with the observations, as shown in Figs. 6 and 7.

5 Sensitivity to Building-Height Variability

5.1 General characteristics of turbulent flows

We now focus on the overall characteristics of turbulent flows in the CTL and UNI experiments, starting with the differences between the respective experiments.

Figure 8a and b shows the vertical profiles of the space- and time-averaged streamwise velocity component $<\overline{u}>_{all}$ and Reynolds stress $-<\overline{u'w'}>_{all}$ over the entire main region for the CTL and UNI experiments, respectively. Here, the angled brackets denote a spatial average, while the subscript *all* refers to the overall main region. Note that the values are normalized by the mean streamwise velocity component U_∞ at the height of the boundary-layer (δ). The mean streamwise velocity components above height $z = h_{all}$ (i.e., above the canopy layer) are lower in the CTL experiment than in the UNI experiment. In contrast, the velocities below height $z = h_{all}$ for the CTL experiment are higher than in the UNI experiment. The Reynolds stress above height $z = h_{all}$ in the CTL experiment is larger than that in UNI experiment. Furthermore, the level of peak Reynolds stress is higher in the CTL experiment than in the UNI experiment.

These differences between the CTL and UNI results can be attributed to the effects of building-height variability. Using the LES results of flows over idealized arrays of roughness blocks, Nakayama et al. (2011) showed that the mean velocity above the building height decreases with increasing building-height variability, and that the magnitude and height of the peak of the Reynolds stress both increase with building-height variability. Our results in terms of the streamwise velocity component and Reynolds stress are consistent with the results of Nakayama et al. (2011).

Xie et al. (2008) carried out an LES investigation over block arrays with random and uniform heights, and found that both types of arrays produced similar turbulent kinetic energies below the average building height. The Reynolds stresses produced in the CTL and UNI experiments below height $z = h_{all}$ are consistent with their results. From Fig. 8b, it is seen that the Reynolds stress in the UNI experiment sharply increases around height $z = h_{all}$, which is likely caused by the presence of the uniform tops of buildings in the UNI experiment, resulting in sharp wind shear and the generation of turbulence.

In Coceal et al. (2006), the velocity components u_i were decomposed as

$$u_i =< \overline{u}_i > + \overline{u}_i'' + u_i', \tag{10}$$

where $< \overline{u}_i >$ are the time- and space-averaged velocities, $\overline{u}_i''$ is the spatial variation of the time-averaged velocity, and u_i' is the turbulent fluctuation. Coceal et al. (2006) showed that dispersive flux, which is defined as $< \overline{u}''\overline{w}'' >$, significantly contributes to the total momentum flux in the canopy layer in which the time-averaged velocities are spatially inhomogeneous. The vertical profiles of the dispersive flux normalized by U_∞ in the CTL and UNI experiments are shown in Fig. 8c. Although the dispersive fluxes for both experiments have peaks just below height $z = h_{all}$, the magnitude of the peak in the UNI experiment is larger than that in the CTL experiment. The UNI profile decreases sharply with height above the height of the peak. Above height $z = h_{all}$, the dispersive flux in the CTL experiment is larger than that in the UNI experiment up to about height $z = 3.5h_{all}$. Xie et al. (2008) performed an LES investigation to compare the dispersive flux in random and uniform block arrays. Their results suggest that both types of dispersive flux have peaks near the average building height, that the peaks obtained from uniform block arrays are stronger than those for random block arrays, and that the dispersive flux of uniform block arrays decreases much more abruptly with increasing height above the height of the peak than that of random block arrays. These characteristics are qualitatively consistent with our results. The dispersive fluxes in both the CTL and UNI experiments appear not to decrease linearly with height because the time-averaged velocities are not spatially homogeneous at heights above the canopy layer. Based on the results shown in Fig. 8a and b, we focus on the height of $z = 0.5h_{all}$ at which the difference between the CTL and UNI experiments is small, and the height of $z = 2.5h_{all}$ where clear differences are seen between the respective experiments.

Figure 9 shows the fields of time-averaged streamwise velocity component normalized by U_∞ for the CTL and UNI experiments over an upstream region ($x = 1 - 5$ km) in which the business districts are located. The difference between the respective experimental results for the region appears to be small at height $z = 0.5h_{all}$ except in areas along a major street around $y = 1.3$ km. This is likely caused by a stronger convergence of the streamwise velocity components on the street in the UNI experiment owing to enhancements arising from the presence of uniform-height buildings (i.e., in the UNI experiment, all lower building heights are raised to $z = h_{all}$). The velocity-deficit regions are reproduced at height $z = 2.5h_{all}$ behind buildings in the CTL experiment, which contrasts to the smooth field of time-averaged streamwise velocity components at height $z = 2.5h_{all}$ in the UNI experiment.

Figure 10 shows the fields of Reynolds stress normalized by U_∞ for the CTL and UNI experiments over the upstream region. While the features are quite similar at height $z = 0.5h_{all}$, the field at height $z = 2.5h_{all}$ in the CTL results has larger values behind the buildings than in the UNI results, which indicates the important role of sparsely and randomly distributed buildings at and above height $z = 2.5h_{all}$ in generating turbulence in the CTL experiment.

5.2 Analysis of Roughness Parameter

To quantitatively reveal the effects of building-height variability, we examined the relationships between the turbulent statistics and roughness parameters. The plan-area index λ_p is used for this analysis because the CTL and UNI experiments have the same values for this parameter. Turbulent statistics were derived in each 1 km by 1 km area in a manner similar to that used to find the roughness parameters in Sect. 2.

5.2.1 Reynolds stress

Figure 11 shows how the Reynolds stress normalized by U_∞ in the CTL and UNI experiments changes as a function of λ_p at the heights of $z = 0.5h_{all}$ and $z = 2.5h_{all}$. The brackets with subscript 1 km^2 indicate spatial averaging over a 1 km by 1 km area. The Reynolds stress at height $z = 0.5h_{all}$ is very similar for the two experiments, which is consistent with the features shown in Fig. 10a and b. By contrast, the values at height $z = 2.5h_{all}$ in the CTL experiment increase with λ_p, while those in the UNI experiment are nearly independent of λ_p. In addition, the differences between the CTL and UNI results at height $z = 2.5h_{all}$ are more apparent when $\lambda_p > 0.32$.

As shown in Figs. 9 and 10, the difference between the CTL and UNI experiments in terms of building distributions at height $z = 2.5h_{all}$ has a significant effect on the turbulent flow results. To interpret this difference, we calculated the respective plan-area indices λ_p at this altitude; i.e., for each experiment, if the building height in a grid cell is below $z = 2.5h_{all}$, the grid cell is regarded as having no buildings. Figure 12a and b shows λ_p at heights $z = 0.5h_{all}$ (denoted by $\lambda_{p,\ 0.5h_{all}}$) and $z = 2.5h_{all}$ ($\lambda_{p,\ 2.5h_{all}}$), respectively, plotted against λ_p at the surface for both the CTL and UNI experiments. Note that, in the UNI experiment, the value of $\lambda_{p,\ 0.5h_{all}}$ is the same as that of λ_p at the surface, and that $\lambda_{p,\ 2.5h_{all}}$ is zero for this experiment. The difference between the CTL and UNI experiments in terms of $\lambda_{p,\ 0.5h_{all}}$ is not very large, confirming the similarity of the respective Reynolds stresses at height $z = 0.5h_{all}$ in Fig. 10. In the CTL experiment, $\lambda_{p,\ 2.5h_{all}}$ rapidly increases if λ_p exceeds 0.32, which appears to be consistent with the Reynolds-stress feature in the CTL experiment at height $z = 2.5h_{all}$ as seen in Fig. 10. Based on these results, we suggest that the Reynolds stress from the CTL experiment at height $z = 2.5h_{all}$ becomes stronger at $\lambda_p > 0.32$ because some building clusters are still present at height $z = 2.5h_{all}$ in this experiment.

The frontal-area index λ_f is another important parameter for describing the geometrical characteristics of urban areas. Here we examine the frontal area of buildings above the height h_{all}. Figure 12c shows λ_f above height $z = h_{all}$ ($\lambda_{f,\ h_{all}}$) plotted against λ_p for the CTL experiment (the figure does not include the corresponding values for the UNI experiment owing to the absence of buildings at that altitude). It is seen that $\lambda_{f,\ h_{all}}$ increases with λ_p, and sharply increases when $\lambda_p > 0.32$. These features agree well with the characteristics determined above for $\lambda_{p,\ 2.5h_{all}}$ and the Reynolds stress. According to these results, the effects of building-height variability on the Reynolds stress increase with λ_p when λ_p is greater than 0.32, and are closely linked to the higher values of $\lambda_{p,\ 2.5h_{all}}$ and $\lambda_{f,\ h_{all}}$ at such values of λ_p.

Interestingly, Zaki et al. (2011) found that the drag coefficient C_d in wind-tunnel experiments, which is relevant to the Reynolds stress, increases with λ_p when $\lambda_p > 0.32$ in flows over block arrays with random heights. A similar feature can also be found for the Reynolds stress and C_d in the LES investigation by Nakayama et al. (2011). According to Zaki et al. (2011), this is because taller buildings, which contribute largely to the total drag in a block array (Xie et al., 2008), tend to be sparsely distributed and, therefore, despite the increase in λ_p, the flow pattern does not enter a skimming flow regime (Oke, 1988). Based on these previous studies and our results, $\lambda_p \approx 0.3$ can be regarded as a threshold at which the effects of building-height variability on the turbulent flow become apparent in various cities.

5.2.2 Momentum transfer according to a quadrant analysis

As described in Sect. 1, turbulent coherent structures over urban surfaces are related to the physical process of turbulent momentum transfer. A quadrant analysis is a useful method for identifying the characteristics of the momentum transfer associated with coherent structures, and has been used in numerous studies of wall turbulence (Wallace, 2016). This method divides the Reynolds stress into four components based on the signs of u' and w': outwards interaction (quadrant 1, $u' > 0,\ w' > 0$); ejection (quadrant 2, $u' < 0,\ w' > 0$); inwards interaction (quadrant 3, $u' < 0,\ w' < 0$) and sweep (quadrant 4, $u' > 0,\ w' < 0$). Raupach (1981) introduced a conditional averaging using the threshold H to investigate the contribution to the Reynolds stress from the ith quadrant as

$$< u'w' >_{i,\ H} = \lim_{T\to\infty} \frac{1}{T} \int_0^T u'(t)w'(t) I_{i,\ H}[u'(t), w'(t)]dt, \tag{11}$$

where the trigger indicator $I_{i,\ H}$ is defined as

$$I_{i,\ H}(u', w') = \begin{cases} 1, \text{ if } (u', w') \text{ is in quadrant } i \text{ and if } |u'w'| \geq H|\overline{u'w'}|, \\ 0, \text{ otherwise.} \end{cases} \tag{12}$$

The fraction of stress exceeding the threshold, which indicates the relative quantity of the ith quadrant, is

$$S_{i,\ H} =< u'w' >_{i,\ H} / \overline{u'w'}. \tag{13}$$

It is noted that the relationship

$$S_{1,\ 0} + S_{2,\ 0} + S_{3,\ 0} + S_{4,\ 0} = 1 \tag{14}$$

holds only for $H = 0$. When the Reynolds stress is negative (as is normally seen in the boundary layer), $S_{2,\ 0}$ and $S_{4,\ 0}$ are positive, while $S_{1,\ 0}$ and $S_{3,\ 0}$ are negative.

Ejections and sweeps contribute to the downwards momentum flux, and are considered to be associated with organized turbulent motions as indicated in Sect. 1. Thus, the magnitude of ejections and sweeps is a good indicator for determining the characteristics of turbulent flows.

To further reveal the relative roles of ejections and sweeps in vertical momentum transfer, we introduce the two parameters

$$\Delta S_0 = S_{4,0} - S_{2,0}, \tag{15}$$

$$Ex = (S_{1,0} + S_{3,0})/(S_{2,0} + S_{4,0}), \tag{16}$$

where ΔS_0 is the difference between sweeps and ejections, and Ex, which is called the exuberance (Shaw et al., 1983), is the ratio of unorganized (S_1 and S_3) motions to organized (S_2 and S_4) motions. The exuberance indicates the efficiency of the vertical momentum flux. Christen et al. (2007) used these parameters to investigate vertical momentum exchange in an urban district and elucidated the roles of coherent structures in momentum transport.

Figure 13 shows the vertical profiles of ΔS_0 and Ex for the CTL and UNI experiments, which are averaged temporally and spatially in a manner similar to the profiles in Fig. 8, where ΔS_0 in the CTL experiment is generally larger than in the UNI experiment, except for heights around h_{all}. This feature of ΔS_0 contrasts to the vertical profile of the Reynolds stress shown in Fig. 8b, which indicates that the Reynolds stress is nearly identical in the CTL and UNI experiments below height $z = 0.5h_{all}$. This suggests that, despite the similarities in the Reynolds stress seen in the two experiments, the building-height variability in the CTL experiment changes the ratio of ejections to sweeps within the building canopy layer. In the upper layer from heights $z = 2.5h_{all}$ to $z = 10h_{all}$, both ΔS_0 and the Reynolds stress are larger in the CTL experiment than in the UNI experiment. We consider that the increased Reynolds stress in this upper layer in the CTL experiment is caused by a sweep-dominated vertical flux.

Figure 13b shows the value of Ex below $z = 2.5h_{all}$ in the CTL experiment to be smaller than that in the UNI experiment. Below $z = 0.5h_{all}$, the decrease in Ex appears to be more pronounced in the CTL experiment than in the UNI experiment even though the respective Reynolds stresses are similar, as shown in Fig. 8b. This indicates that the efficiency of the vertical momentum flux in the canopy layer is reduced by building-height variability. In contrast, the values of Ex in the CTL and UNI experiments are very similar at altitudes above height $z = 2.5h_{all}$, indicating that the efficiency of the momentum flux above these altitudes is similar for both experiments.

Based on the differences between the vertical profiles shown in Fig. 13, we focus on the heights $z = 0.5h_{all}$ and $z = 2.5h_{all}$ to reveal the relationship between building-height variability and turbulent-flow characteristics. Figure 14a and b shows variations in ΔS_0 against λ_p in the CTL and UNI experiments at these two altitudes. At height $z = 0.5h_{all}$, sweeps are dominant among the contributions to the Reynolds stress for both experiments, which is consistent with previous results showing a stronger contribution of sweeps to the total momentum flux than ejections near and below the tops of block arrays (Raupach 1981; Coceal et al. 2007a). From Fig. 13a, it is seen that the contribution of sweeps in the CTL experiment is larger than in the UNI experiment. By contrast, the value of ΔS_0 at height $z = 0.5h_{all}$ appears to be independent of λ_p in both experiments. However, at height $z = 2.5h_{all}$, the value of ΔS_0 in the CTL experiment increases with λ_p when $\lambda_p > 0.32$, while in the UNI experiment, it is independent of λ_p. The increase in ΔS_0 in the CTL experiment is consistent with the Reynolds-stress results shown Fig. 11b, thus suggesting that sweeps contribute to the increase in Reynolds stress for $\lambda_p > 0.32$. Similar results were noted by Kanda (2006).

Figure 14c and d shows Ex plotted against λ_p in the CTL and UNI experiments at heights $z = 0.5$ and $2.5h_{all}$, respectively, where the difference in the value of Ex at height $z = 0.5h_{all}$ increases with λ_p, suggesting the dominance of unorganized structures as λ_p increases. As shown in Fig. 13b, at height $z = 2.5h_{all}$ the values of Ex in both experiments are practically independent of λ_p.

By setting H in Eq. 12 to a value larger than zero, we evaluate the extent to which extreme instantaneous momentum fluxes contribute to the total Reynolds stress in a certain period. We define the percentage contribution to the Reynolds stress of a value of $u'w'$ larger than the Reynolds stress by a factor of H using

$$E_H \equiv \sum_{i=1}^{4} S_{i,\ H} = \sum_{i=1}^{4} < u'w' >_{i,\ H} / \overline{u'w'}. \tag{17}$$

Unlike in Raupach (1981) in which each component of the momentum flux was evaluated, all of the components in Eq. 17 are added to assess the total of the extreme momentum fluxes. We set $H = 20$ here to extract extreme values of $u'w'$, with qualitatively similar results also found with $H = 15$ and H =10. Thus, $H =$ 20 is assumed to be a representative value.

Figure 14e and f shows the variations of E_{20} with λ_p at heights $z = 0.5$ and $z = 2.5h_{all}$, respectively, for both experiments. The results at height $z = 0.5h_{all}$ reveal small differences between the CTL and UNI experiments and are, in general, larger than those at height $z = 2.5h_{all}$. This indicates that the flow is highly turbulent at height $z = 0.5h_{all}$, and that the extreme values of the momentum flux contribute more significantly to the total momentum flux at this altitude. However, as the magnitude of $u'w'$ itself is low at height $z = 0.5h_{all}$, the effects of the fluctuation itself may not be very strong. It is seen that, at height $z = 2.5h_{all}$, the value of E_{20} in the CTL experiment increases with λ_p, but is independent of λ_p in the UNI experiment. Moreover, the shape of the relationship between E_{20} at height $z = 2.5h_{all}$ and λ_p in the CTL experiment appears to be quite similar to that between $\lambda_{p,\ 2.5h_{all}}$ and λ_p shown in Fig. 12b. This suggests that increasing the number of buildings at height $z = 2.5h_{all}$ generates highly turbulent flows at higher values of λ_p.

The increase in the contribution from extreme values of $u'w'$ to the Reynolds stress at height $z = 2.5h_{all}$ in the CTL experiment occurs because the building-height variability in this experiment leads to a higher momentum flux at this altitude as clearly indicated in Fig. 15a, which shows the horizontal cross-section of E_{20} over a 1 km by 1 km area within one of the business districts. It is seen that high values of E_{20} appear in areas around randomly and sparsely distributed buildings. In contrast, areas with higher E_{20} values also correspond to areas with a weak Reynolds stress and small value of Ex (see Fig. 15b and c), which indicates the small contribution of the extreme momentum flux around buildings to the total momentum flux, and is not related to organized turbulent motion. From the features demonstrated in Figs. 14 and 15, it is seen that the turbulent flow characteristics and contributions of extreme momentum fluxes are significantly influenced by the presence of buildings with significant height variability.

We have shown the qualitative consistency of the Reynolds stress and quadrant analysis results, if averaged both in time and space, with that over block arrays with variable height. In contrast, the inhomogeneous profiles of the turbulent-flow characteristics (Fig. 15) suggest that the local characteristics of the turbulent flow over urban surfaces are significantly influenced by the inhomogeneity of actual urban buildings, and would not be expected to be similar to that over idealized block arrays.

6 Summary and Conclusions

An LES investigation of the turbulent flow over the city of Kyoto has been conducted to investigate the effects of building-height variability on the turbulence in the lower part of the urban boundary layer. A digital surface model data has reproduced the actual buildings of Kyoto in the LES model.

We used roughness parameters such as H_{ave}, σ_H, λ_p, and λ_f to evaluate the morphological characteristics of buildings, and compared these parameters with those derived for Tokyo, Nagoya as well as for North American and European cities. For $\lambda_p > 0.3$, the value of λ_f for Kyoto is small compared with the empirical values for Tokyo and Nagoya, but similar to those obtained for European cities. The relationship between H_{ave} and σ_H in Kyoto agrees closely with the empirical profile. From these comparisons, the building morphological characteristics of Kyoto indicate a dense distribution, and buildings with a variety of heights.

We compared the LES results with observations of atmospheric turbulence obtained using a sonic anemometer and a Doppler lidar at the Ujigawa Open Laboratory, which is an area included in the main region of the LES model. For this comparison, certain periods were extracted from the total set of observations to meet the weather conditions assumed in the LES model. The model is to reproduce the observed characteristics of turbulence up to a height of about 150 m.

We carried out two experiments: one modelling the actual buildings of Kyoto (CTL), and one (UNI) in which all building heights were set to the average building height in the main region of the city h_{all}. We find small differences between the CTL and UNI experiments in terms of the mean streamwise velocity component and the Reynolds stress at height $z = 0.5h_{all}$, but large differences at height $z = 2.5h_{all}$. The spatial fields of time-averaged streamwise velocity components and Reynolds stresses produced in the CTL experiment indicate regions of reduced velocity and strong Reynolds stress behind sparsely and randomly distributed buildings at height $z = 2.5h_{all}$; this contrasts with the UNI results, in which these fields at height $z = 2.5h_{all}$ are smooth. We investigated the relationships between turbulent statistics and λ_p evaluated over 1 km by 1 km areas to reveal the differences between the CTL and UNI experiments. The Reynolds stress in the CTL experiment at height $z = 2.5h_{all}$ is larger than that in the UNI experiment when $\lambda_p > 0.32$, while the Reynolds stress at height $z = 0.5h_{all}$ is similar for both experiments. We suggest that the increase in the Reynolds stress at height $z = 2.5h_{all}$ is caused by the presence of some building clusters at height $z = 2.5h_{all}$ in the CTL experiment, and that a value of λ_p of about 0.3 is the threshold above which the effects of building-height variability become obvious over various urban surfaces.

A quadrant analysis was used to investigate the characteristics of turbulent coherent flows. Sweeps in the CTL experiment at height $z = 2.5h_{all}$ are found to increase with λ_p for $\lambda_p > 0.32$, which is similar to that seen in the Reynolds stress for $\lambda_p > 0.32$, suggesting the increase in Reynolds stress is caused by the presence of sweeps. The vertical momentum flux in the CTL experiment is less efficient than that in the UNI experiment at height $z = 0.5h_{all}$, which indicates that the building-height variability in the CTL experiment reduces the efficiency of the flux in the canopy layer.

The contributions of the extreme instantaneous momentum flux to the total Reynolds stress were also investigated. The amount of extreme momentum flux in the CTL experiment at height $z = 2.5h_{all}$ depends strongly on the presence of buildings at this altitude. Examination of horizontal cross-sections reveals that areas with extreme momentum fluxes are distributed around buildings. However, the efficiency of the Reynolds stress and momentum flux are small in areas with an extreme momentum flux, implying its negligible contribution around buildings to the net Reynolds stress, as well as the lack of association with coherent turbulent motions. The relationships between turbulent coherent structures and building-height variability were investigated through the use of space- and time-averaged profiles. However, future research on turbulent coherent structures over urban surfaces should focus on instantaneous and local structures, such as vortex structures behind high, isolated buildings (Park et al., 2015), and flow patterns in block arrays associated with coherent structures above blocks (Inagaki et al., 2012).

Acknowledgements We would like to thank the editor and three anonymous reviewers for their helpful comments and suggestions. We would like to express our deepest gratitude to Dr. Wim Vanderbauwhede at the University of Glasgow, who helped to create an MPI version of the code. We thank Dr. Hiromasa Nakayama at the Japan Atomic Energy Agency for his guidance on the LES modelling. We would like to thank the support by Prof. Hajime Nakagawa of Kyoto University for conducting the field measurements at the Ujigawa Open Laboratory. This research partly used computational resources under the Collaborative Research Program for Young Scientists provided by the Academic Centre for Computing and Media Studies, Kyoto University. This study was supported by JSPS Kakenhi grant numbers 26282107 and 16H01846, and DPRI Collaborative Research 28H-04 and 29S-01.

References

Bou-Zeid E, Overney J, Rogers BD, Parlange MB (2009) The effects of building representation and clustering in large-eddy simulations of flows in urban canopies. Boundary-Layer Meteorol 132(3):415–436

Cañadillas B, Westerhellweg A, Neumann T (2011) Testing the performance of a ground-based wind lidar system: One year intercomparison at the offshore platform fino1. Dewi Mag 38:58–64

Cheng H, Castro IP (2002) Near wall flow over urban-like roughness. Boundary-Layer Meteorol 104(2):229–259

Chorin AJ (1967) A numerical method for solving incompressible viscous flow problems. J Comput Phys 2(1):12–26

Christen A, van Gorsel E, Vogt R (2007) Coherent structures in urban roughness sublayer turbulence. Int J Climatol 27(14):1955–1968

Coceal O, Thomas T, Castro I, Belcher S (2006) Mean flow and turbulence statistics over groups of urban-like cubical obstacles. Boundary-Layer Meteorol 121(3):491–519

Coceal O, Dobre A, Thomas T, Belcher S (2007a) Structure of turbulent flow over regular arrays of cubical roughness. J Fluid Mech 589:375–409

Coceal O, Dobre A, Thomas TG (2007b) Unsteady dynamics and organized structures from dns over an idealized building canopy. Int J Climatol 27(14):1943–1953

Counihan J (1975) Adiabatic atmospheric boundary layers: a review and analysis of data from the period 1880–1972. Atmos Environ 9(10):871–905

ESDU (1985) Characteristics of atmospheric turbulence near the ground. part ii: single point data for strong winds (neutral atmosphere). ESDU International, London

Giometto M, Christen A, Meneveau C, Fang J, Krafczyk M, Parlange M (2016) Spatial characteristics of roughness sublayer mean flow and turbulence over a realistic urban surface. Boundary-Layer Meteorol 160(3):425–452

Goldstein D, Handler R, Sirovich L (1993) Modeling a no-slip flow boundary with an external force field. J Comput Phys 105(2):354–366

Inagaki A, Castillo MCL, Yamashita Y, Kanda M, Takimoto H (2012) Large-eddy simulation of coherent flow structures within a cubical canopy. Boundary-Layer Meteorol 142(2):207–222

Kaimal J, Wyngaard J, Izumi Y, Coté O (1972) Spectral characteristics of surface-layer turbulence. Q J R Meteorol Soc 98(417):563–589

Kanda M (2006) Large-eddy simulations on the effects of surface geometry of building arrays on turbulent organized structures. Boundary-Layer Meteorol 118(1):151–168

Kanda M, Moriwaki R, Kasamatsu F (2004) Large-eddy simulation of turbulent organized structures within and above explicitly resolved cube arrays. Boundary-Layer Meteorol 112(2):343–368

Kanda M, Inagaki A, Miyamoto T, Gryschka M, Raasch S (2013) A new aerodynamic parametrization for real urban surfaces. Boundary-Layer Meteorol 148(2):357–377

Macdonald R, Griffiths R, Hall D (1998) An improved method for the estimation of surface roughness of obstacle arrays. Atmos Environ 32(11):1857–1864

Nakajima C, Mitsuta Y, Tanaka M (1979) Ujigawa meteorological tower for boundary layer monitoring. Annuals of Disaster Prevention Research Institute 22B(2):127–141

Nakayama H, Takemi T, Nagai H (2011) Les analysis of the aerodynamic surface properties for turbulent flows over building arrays with various geometries. J Appl Meteorol Clim 50(8):1692–1712

Nakayama H, Takemi T, Nagai H (2012) Large-eddy simulation of urban boundary-layer flows by generating turbulent inflows from mesoscale meteorological simulations. Atmos Sci Lett 13(3):180–186

Nakayama H, Leitl B, Harms F, Nagai H (2014) Development of local-scale high-resolution atmospheric dispersion model using large-eddy simulation. part 4: turbulent flows and plume dispersion in an actual urban area. J Nucl Sci Technol 51(5):626–638

Nakayama H, Takemi T, Nagai H (2015) Large-eddy simulation of turbulent winds during the fukushima daiichi nuclear power plant accident by coupling with a meso-scale meteorological simulation model. Adv Sci Res 12(1):127–133

Nakayama H, Takemi T, Nagai H (2016) Development of lo cal-scale h igh-resolution atmospheric di spersion m odel using l arge-e ddy s imulation. part 5: detailed simulation of turbulent flows and plume dispersion in an actual urban area under real meteorological conditions. J Nucl Sci Technol 53(6):887–908

Oikawa S, Meng Y (1995) Turbulence characteristics and organized motion in a suburban roughness sublayer. Boundary-Layer Meteorol 74(3):289–312

Oke TR (1988) Street design and urban canopy layer climate. Energy Buil 11(1):103–113

Park SB, Baik JJ, Han BS (2015) Large-eddy simulation of turbulent flow in a densely built-up urban area. Environ Fluid Mech 15(2):235–250

Ratti C, Di Sabatino S, Britter R, Brown M, Caton F, Burian S (2002) Analysis of 3-d urban databases with respect to pollution dispersion for a number of european and american cities. Water Air Soil Pollut Focus 2(5-6):459–469

Raupach M (1981) Conditional statistics of reynolds stress in rough-wall and smooth-wall turbulent boundary layers. J Fluid Mech 108:363–382

Roth M (2000) Review of atmospheric turbulence over cities. Q J R Meteorol Soc 126(564):941–990

Shaw RH, Tavangar J, Ward DP (1983) Structure of the reynolds stress in a canopy layer. J Clim Appl Meteorol 22(11):1922–1931

Smagorinsky J (1963) General circulation experiments with the primitive equations: I. the basic experiment. Mon Weather Rev 91(3):99–164

Stoll R, Porté-Agel F (2006) Effect of roughness on surface boundary conditions for large-eddy simulation. Boundary-Layer Meteorol 118(1):169–187

Wallace JM (2016) Quadrant analysis in turbulence research: history and evolution. Annu Rev Fluid Mech 48:131–158

Xie ZT (2011) Modelling street-scale flow and dispersion in realistic windstowards coupling with mesoscale meteorological models. Boundary-Layer Meteorol 141(1):53–75

Xie ZT, Castro IP (2009) Large-eddy simulation for flow and dispersion in urban streets. Atmos Environ 43(13):2174–2185

Xie ZT, Coceal O, Castro IP (2008) Large-eddy simulation of flows over random urban-like obstacles. Boundary-Layer Meteorol 129(1):1–23

Zaki SA, Hagishima A, Tanimoto J, Ikegaya N (2011) Aerodynamic parameters of urban building arrays with random geometries. Boundary-Layer Meteorol 138(1):99–120

Zhu X, Iungo GV, Leonardi S, Anderson W (2017) Parametric study of urban-like topographic statistical moments relevant to a priori modelling of bulk aerodynamic parameters. Boundary-Layer Meteorol 162:231–253

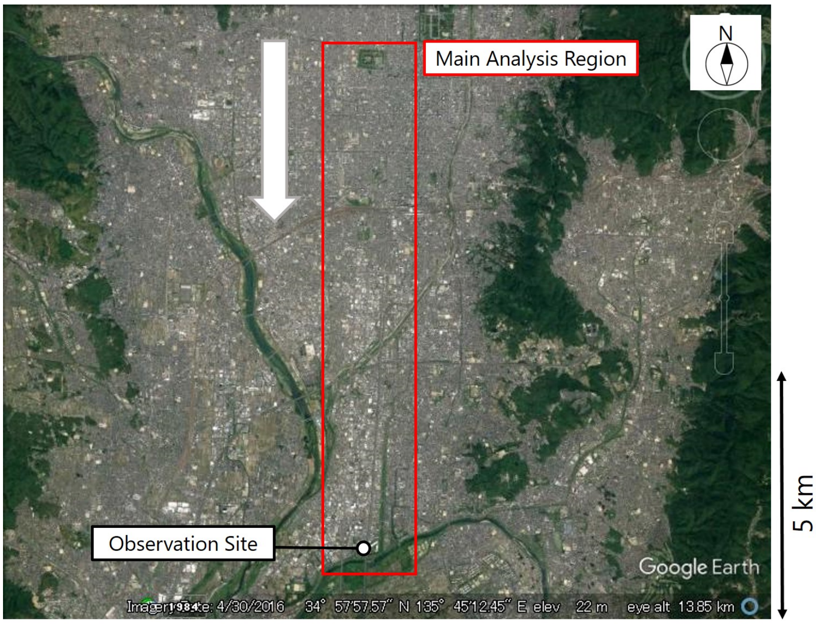

Fig. 1 The study area in which the LES model and observations were carried out is indicated by the red box. The observational site of the Disaster Prevention Research Institute, Kyoto University, is indicated by the white circle. The white arrow indicates the streamwise wind direction. The satellite picture is taken from Google Earth.

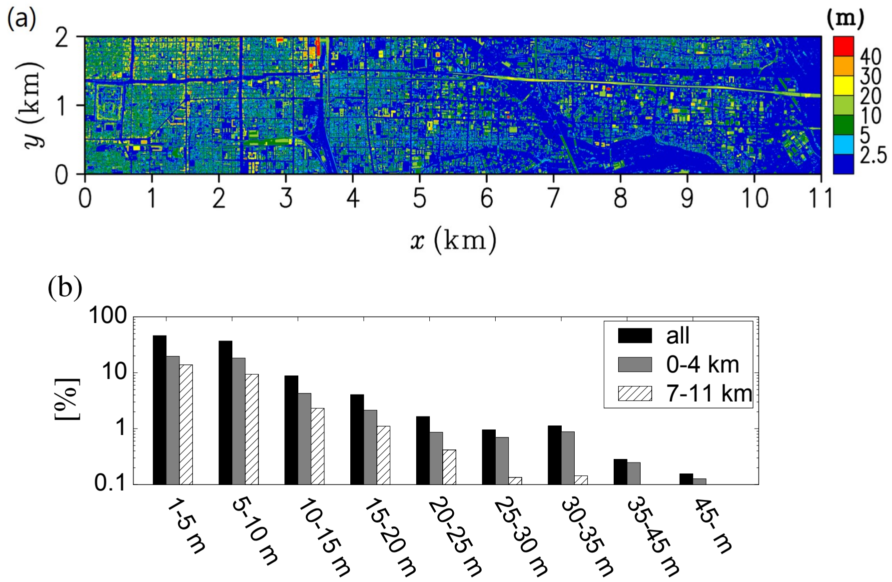

Fig. 2 (a) Distribution of building and structure heights in the analysis region of Kyoto. (b) Frequency distribution of building heights in the analysis region. The black bar indicates the frequency distribution of buildings in the overall region, while the grey and hatched bars indicate the frequency distributions of buildings in the regions with $x = 0 - 4$ km and with $x = 7 - 11$ km, respectively.

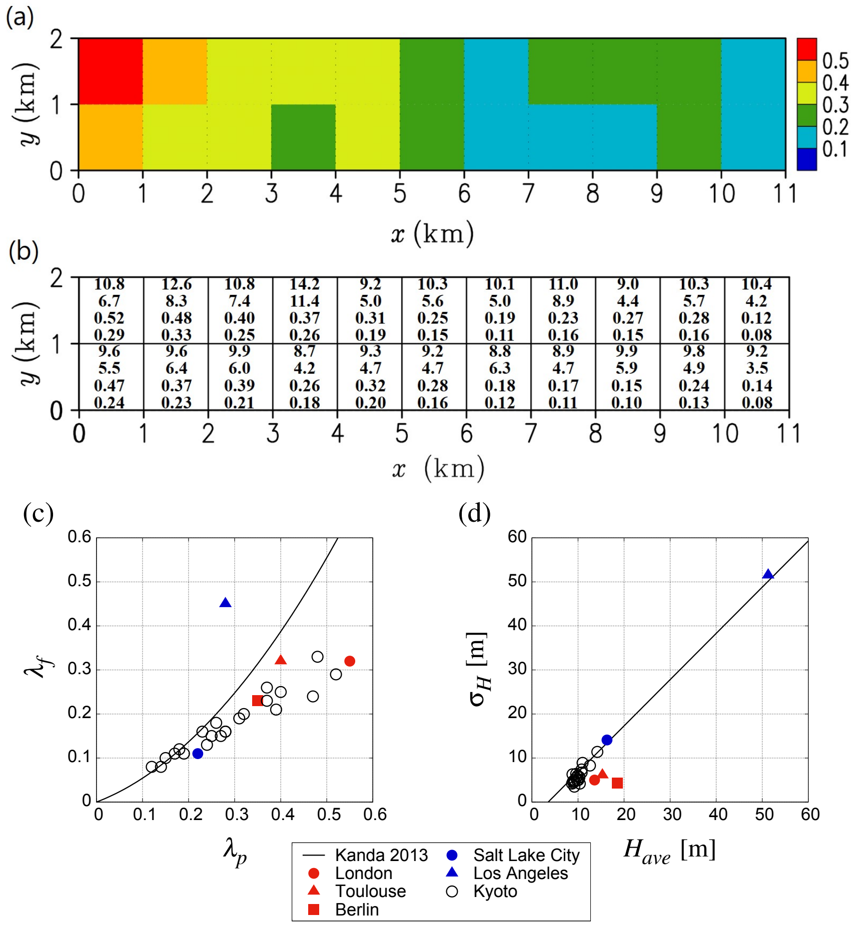

Fig. 3 (a) λ_p calculated for 1 km by 1 km areas over the analysis region. (b) Roughness parameters calculated for 1 km by 1 km areas over the analysis region. In each box, the first row is H_{ave}, the second is σ_H, the third is λ_p, and the fourth is λ_f. Scatter plots (c) between λ_p and λ_f and (d) between σ_H and H_{ave}. The black lines in (c) and (d) indicate the empirical relationships derived from Tokyo and Nagoya, respectively, by Kanda et al. (2013). The values of Salt Lake City and Los Angeles in North America and London, Toulouse, and Berlin in Europe, as indicated by the lower legend, are obtained from Ratti et al. (2002).

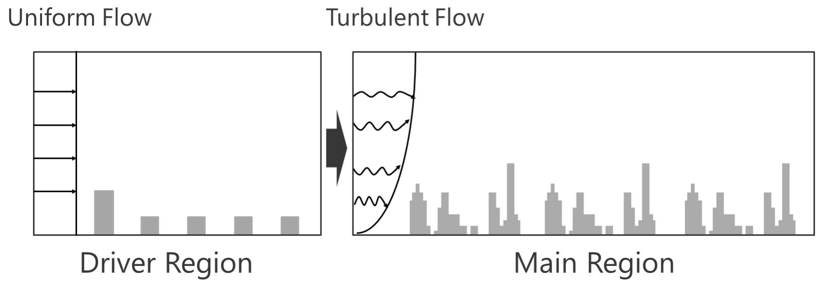

Fig. 4 Schematic of turbulent flows formed in the driver region and imposed on the main region as the inflow condition.

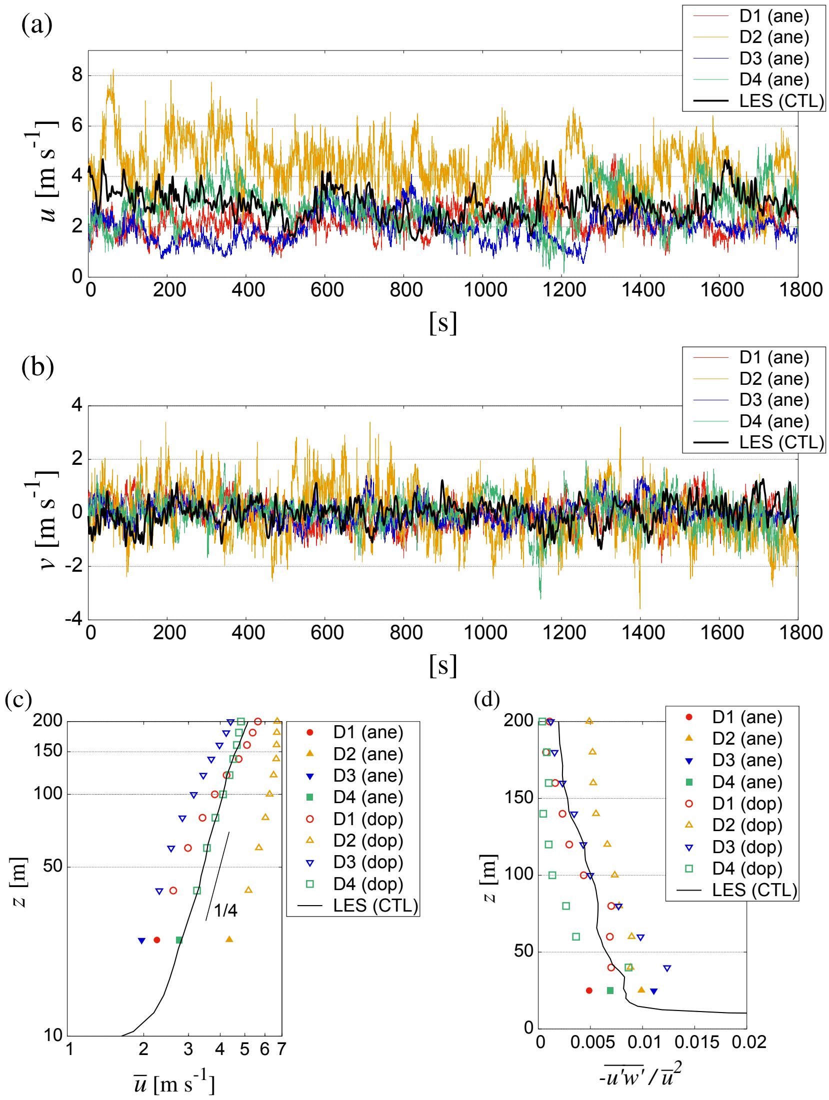

Fig. 5 Time series of (a) streamwise and (b) spanwise velocity components at 25-m height observed by the sonic anemometer during periods D1 – D4 and simulated by the LES model. Vertical profiles of (c) mean streamwise velocity component and (d) Reynolds stress normalized by the mean streamwise velocity component in the observations and the LES results. Note that the profiles in (c) are plotted on logarithmic axes. A line with a slope 1/4 is also plotted for reference. Here, 'ane' and 'dop' refer to the observations by the anemometer and Doppler lidar, respectively.

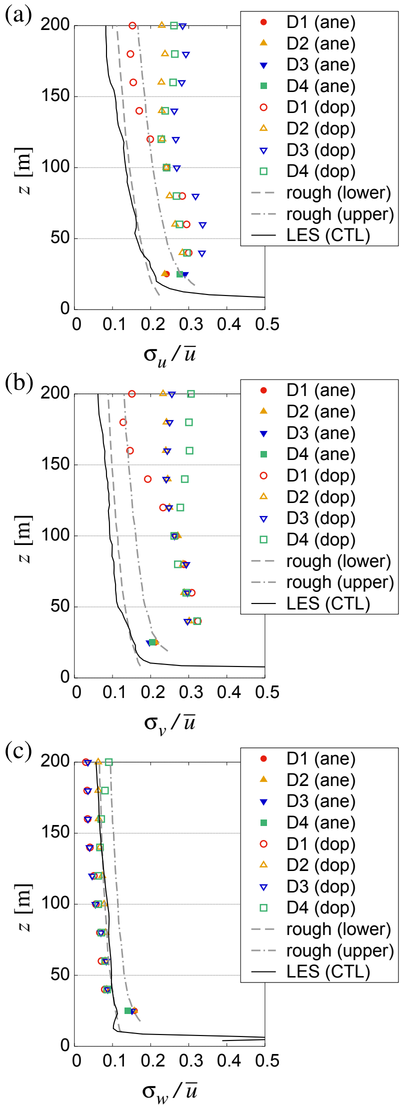

Fig. 6 Vertical profiles of turbulence intensity from the observations, the LES model, and the empirical profiles provided by the ESDU (1985) for the (a) u, (b) v, and (c) w components. The dashed and dashed–dotted lines indicate the upper and the lower limits, respectively, of the rough-surface class based on the ESDU (1985).

.

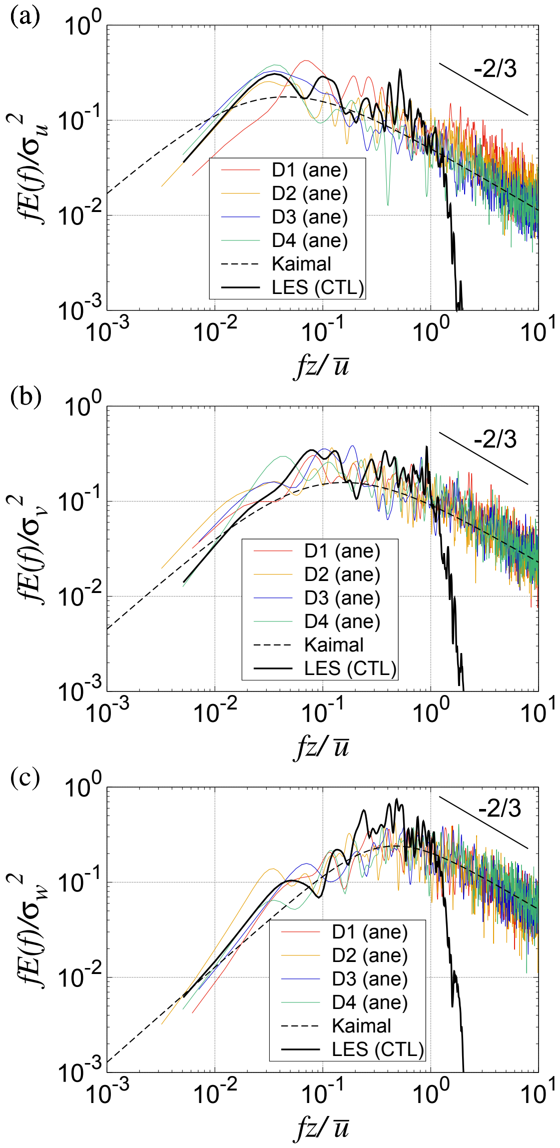

Fig. 7 Power spectra obtained from the sonic anemometer and the LES model at 25-m height plotted on logarithmic axes: (a) u, (b) v, and (c) w components. The dashed line indicates the empirical profile over a rural surface proposed by Kaimal et al. (1972).

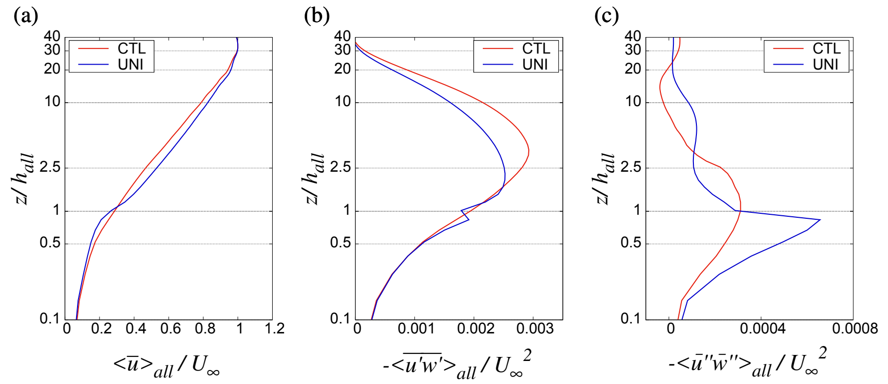

Fig. 8 Vertical profiles of (a) time-averaged streamwise velocity component, (b) Reynolds stress, and (c) dispersive flux averaged spatially over the main region. These values are normalized by U_∞. Red and blue lines denote the result of the CTL and UNI experiments, respectively. The vertical axis is normalized by $z = h_{all}$. Note that a logarithmic scale is used for the vertical axis.

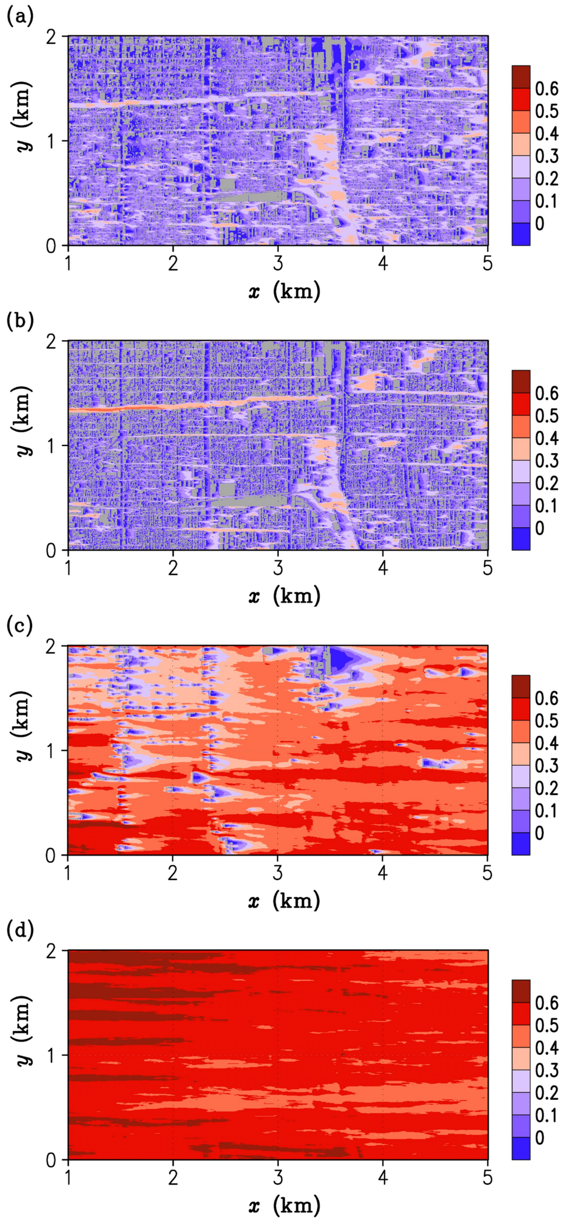

Fig. 9 Horizontal cross sections of the time-averaged streamwise velocity component normalized by U_∞ in (a) the CTL experiment at height $z = 0.5h_{all}$, (b) the UNI experiment at height $z = 0.5h_{all}$, (c) the CTL experiment at height $z = 2.5h_{all}$, and (d) the UNI experiment at height $z = 2.5h_{all}$. An upstream part of the main region is shown. The legend indicating the wind speed is present to the right of each panel. The grey shading indicates buildings.

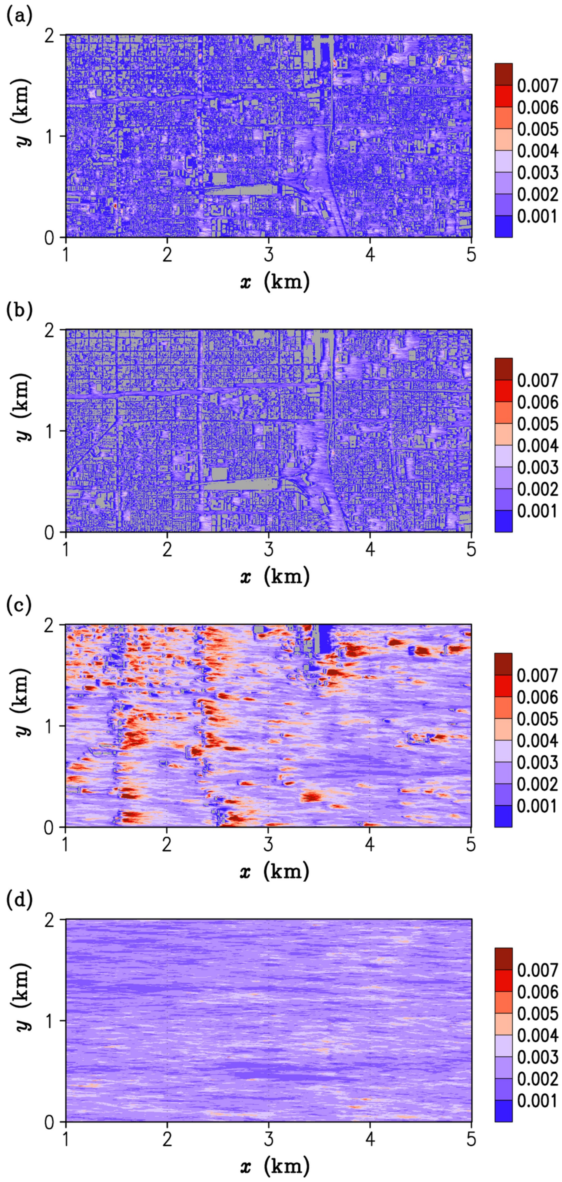

Fig. 10 As Fig. 9, except with the corresponding Reynolds-stress results.

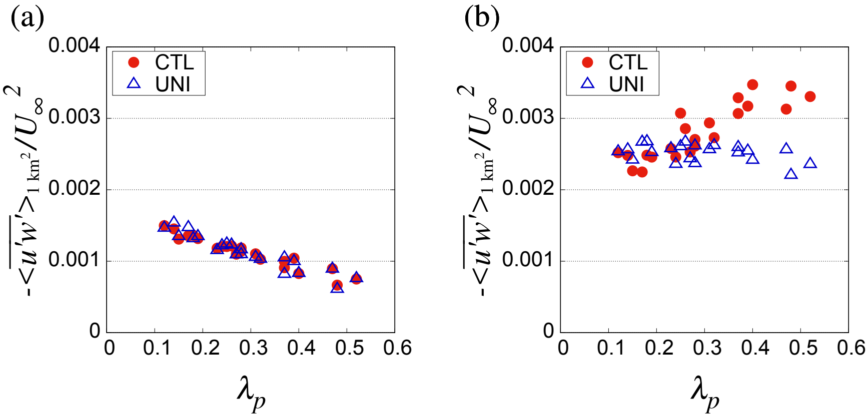

Fig. 11 Variations of Reynolds stress normalized by U_∞ with λ_p at heights (a) $z = 0.5h_{all}$ and (b) $z = 2.5h_{all}$.

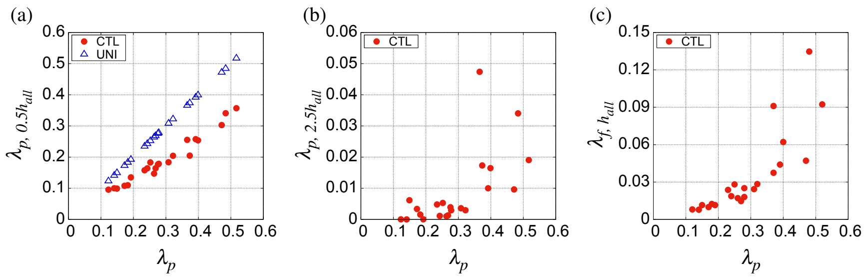

Fig. 12 Variations of λ_p calculated (a) at height $z = 0.5h_{all}$ ($\lambda_{p,\ 0.5h_{all}}$), (b) at height $z = 2.5h_{all}$ ($\lambda_{p,\ 2.5h_{all}}$), and (c) λ_f calculated at height $z = h_{all}$ ($\lambda_{f,\ h_{all}}$) with λ_p at the surface. Note that the scale of the vertical axis differs by panel.

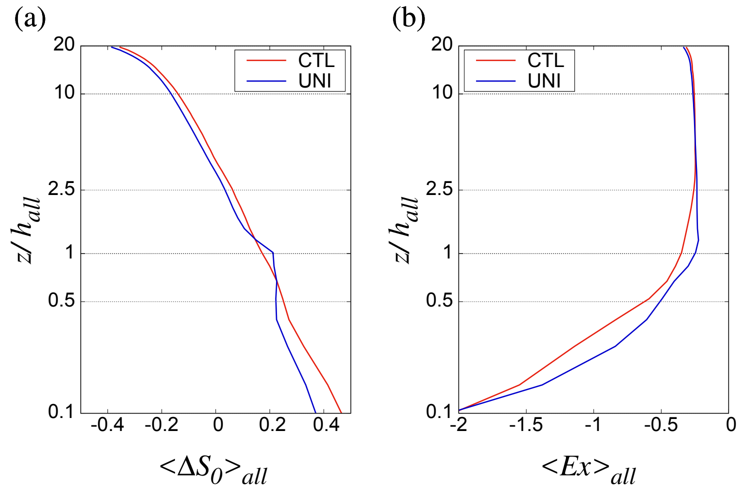

Fig. 13 Vertical profiles of (a) ΔS_0 and (b) Ex averaged spatially over the main region. Red and blue lines denote the results of the CTL and UNI experiments, respectively. The vertical axis is normalized by h_{all}. Note that a logarithmic scale is used for the vertical axis.

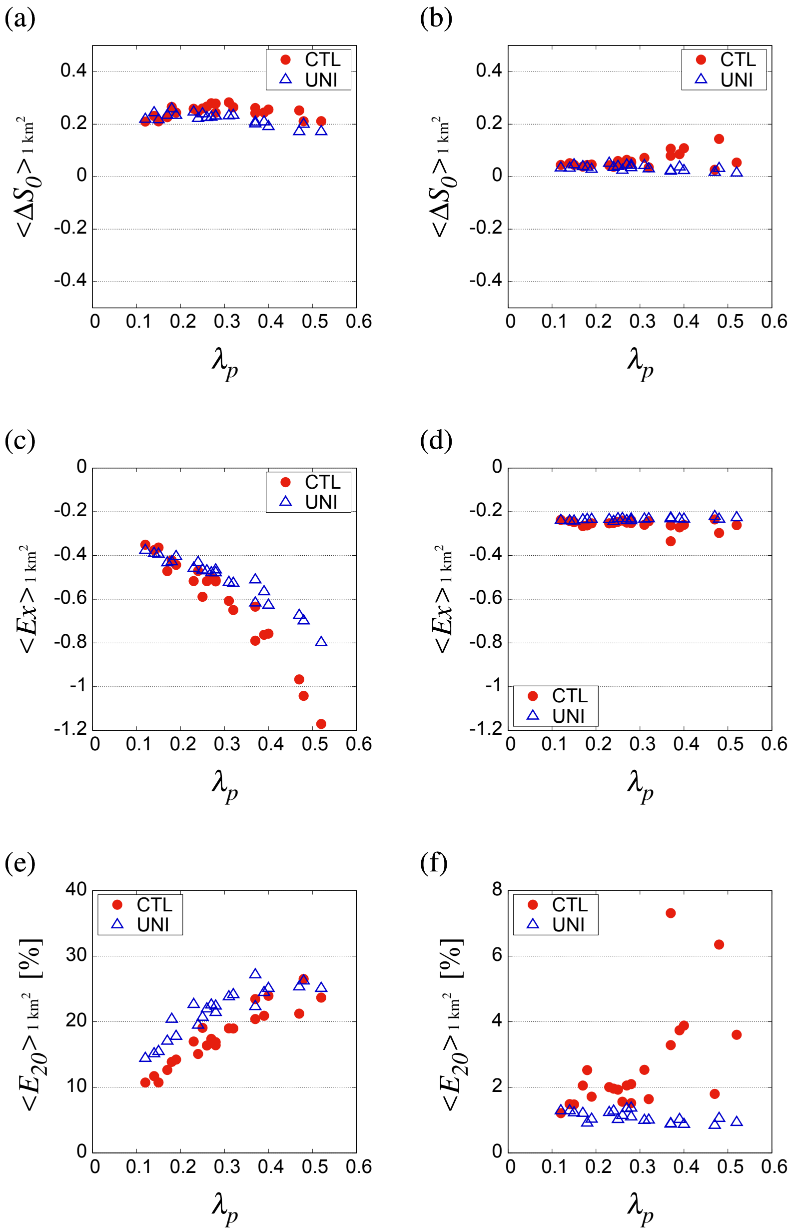

Fig. 14 Variations of ΔS_0 with λ_p at (a) heights $z = 0.5h_{all}$ and (b) $z = 2.5h_{all}$, Ex at (c) heights $z = 0.5h_{all}$ and (d) $z = 2.5h_{all}$, and E_{20} at (e) heights $z = 0.5h_{all}$ and (f) $z = 2.5h_{all}$.

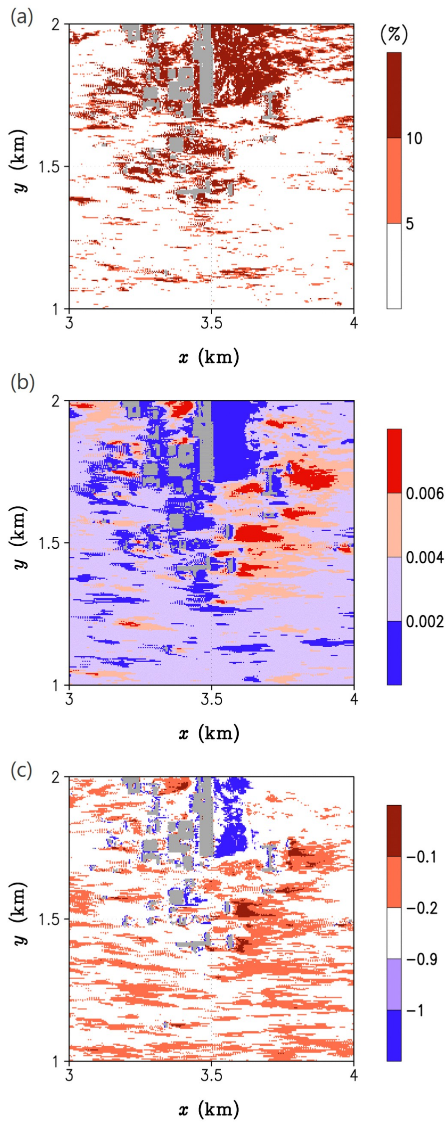

Fig. 15 Horizontal cross section of (a) E_{20}, (b) Reynolds stress normalized by U_∞, and (c) Ex at height $z = 2.5h_{all}$ over a 1 km by 1 km area within the business district in the CTL experiment. The grey shading indicates buildings.